



**HAL**  
open science

## Conical nanopores highlight the pro-aggregating effects of pyrimethanil fungicide on $A\beta(1-42)$ peptides and dimeric splitting phenomena

Nathan Meyer, Nicolas Arroyo, Matteo Baldelli, Nicolas Coquart, Jean-Marc Janot, Véronique Perrier, Mauro Chinappi, Fabien Picaud, Joan Torrent, Sebastien Balme

### ► To cite this version:

Nathan Meyer, Nicolas Arroyo, Matteo Baldelli, Nicolas Coquart, Jean-Marc Janot, et al. Conical nanopores highlight the pro-aggregating effects of pyrimethanil fungicide on  $A\beta(1-42)$  peptides and dimeric splitting phenomena. *Chemosphere*, 2022, 291, pp.132733. 10.1016/j.chemosphere.2021.132733 . hal-03791236

**HAL Id: hal-03791236**

**<https://hal.umontpellier.fr/hal-03791236v1>**

Submitted on 29 Sep 2022

**HAL** is a multi-disciplinary open access archive for the deposit and dissemination of scientific research documents, whether they are published or not. The documents may come from teaching and research institutions in France or abroad, or from public or private research centers.

L'archive ouverte pluridisciplinaire **HAL**, est destinée au dépôt et à la diffusion de documents scientifiques de niveau recherche, publiés ou non, émanant des établissements d'enseignement et de recherche français ou étrangers, des laboratoires publics ou privés.

1 Conical nanopores highlight the pro-aggregating  
2 effects of pyrimethanil fungicide on A $\beta$ (1-42)  
3 peptides and dimeric splitting phenomena

4 *Nathan Meyer<sup>a†</sup>, Nicolas Arroyo<sup>b†</sup>, Matteo Baldelli<sup>c†</sup>, Nicolas Coquart<sup>a</sup>, Jean Marc Janot<sup>a</sup>,*  
5 *Veronique Perrier<sup>d</sup>, Mauro Chinappi<sup>c</sup>, Fabien Picaud<sup>b</sup>, Joan Torrent<sup>d</sup>, Sebastien Balme<sup>a\*</sup>*

6 <sup>a</sup>Institut Européen des Membranes, UMR5635 UM ENCSM CNRS, Place Eugène Bataillon,  
7 34095 Montpellier cedex 5, France.

8 <sup>b</sup>Laboratoire de Nanomédecine, Imagerie et Thérapeutique, EA4662, Université Bourgogne-  
9 Franche-Comté (UFR Sciences et Techniques), Centre Hospitalier Universitaire de Besançon,  
10 16 route de Gray, 25030 Besançon, France

11 <sup>c</sup>Dipartimento di Ingegneria Industriale, Università di Roma Tor Vergata, Via del Politecnico  
12 1, 00133 Roma, Italia

13 <sup>d</sup>INM, University of Montpellier , INSERM, Montpellier, France

14 † equal contribution,

15 \*corresponding authors. Sebastien.balme@umontpellier.fr

16 **Abstract**

17 The A $\beta$ (1-42) aggregation is a key event in the physiopathology of Alzheimer's disease (AD).  
18 Exogenous factors such as environmental pollutants, and more particularly pesticides, can  
19 corrupt A $\beta$ (1-42) assembly and could influence the occurrence and pathophysiology of AD.  
20 However, pesticide involvement in the early stages of A $\beta$ (1-42) aggregation is still unknown.  
21 Here, we employed conical track-etched nanopore in order to analyse the A $\beta$ (1-42) fibril  
22 formation in the presence of pyrimethanil, a widely used fungicide belonging to the  
23 anilinopyrimidine class. Our results evidenced a pro-aggregating effect of pyrimethanil on  
24 A $\beta$ (1-42). A $\beta$ (1-42) assemblies were successfully detected using conical nanopore coated with  
25 PEG. Using an analytical model, the large current blockades observed ( $>0.7$ ) were assigned to  
26 species with size close to the sensing pore. The long dwell times (hundreds ms scale) were  
27 interpreted by the possible interactions amyloid/PEG using molecular dynamic simulation.  
28 Such interaction could leave until splitting phenomena of the dimer structure. Our work also  
29 evidences that the pyrimethanil induce an aggregation of A $\beta$ (1-42) mechanism in two steps  
30 including the reorganization prior the elongation phase.

31 **Keywords:** amyloid, nanopore, resistive pulse, fungicide, A $\beta$ (1-42), track-etched, lag phase,

## 32 **1. Introduction**

33 The assembly of normally soluble proteins into an amyloid fold has become the dominant  
34 model that explains the pathogenesis of numerous neurodegenerative disorders, including  
35 Alzheimer's (AD) and Parkinson's diseases (Chiti and Dobson, 2017; Ke et al., 2020). This  
36 critical misfolding pathway, called amyloidogenesis, is guiding the development of potential  
37 treatments since it generates structurally different protein assemblies that are thought to be  
38 responsible for the cellular toxicity (Soto and Pritzkow, 2018). Although unexpectedly diverse  
39 and complex, the amyloid fold is structurally characterized by a typical cross- $\beta$  fibril  
40 architecture and is often considered to be energetically the most favourable protein state (Gazit,

41 2002). Nevertheless, amyloids are dynamic, with monomers/oligomers association and  
42 dissociation from their ends and surface (Carulla et al., 2010; Jahn and Radford, 2008). In vitro,  
43 kinetic growth curves for A $\beta$ (1-42) fibril formation starting from pure monomer display a  
44 sigmoidal profile, where after a first slow amyloid size increase (lag phase), the aggregates start  
45 to growth (growth phase) until saturation is reached. Oligomeric species populated during the  
46 lag phase are heterogeneous and rapidly evolve to amyloid fibrils during the growth phase, in  
47 which fibril mass increases with time to an equilibrium plateau (Michaels et al., 2018). There  
48 is compelling evidence that different physicochemical factors can influence the duration of the  
49 lag phase. The search for a trigger event leading to an accelerated A $\beta$ (1-42) fibril formation has  
50 mostly been investigated from the perspectives of the properties of A $\beta$  itself (i.e., mutations,  
51 truncations), but marginally from abnormal interactions with exogenous synthetic molecules  
52 (McLaurin et al., 2000).

53 Indeed, environmental pollutants are now suspected to play a role in the aetiology or  
54 incidence of neurological disorders (Chin-Chan et al., 2015). Epidemiological studies revealed  
55 that occupational exposure of farmers to organophosphates has been associated with an  
56 increased risk to develop Alzheimer's disease (Hayden et al., 2010). Three fungicides belonging  
57 to the anilinopyrimidine class, i.e. cyprodinil, mepanipyrim and pyrimethanil are widely used  
58 for crop preservation, as well as for long-term storage of fruits and vegetables. Many reports  
59 have in the past established their presence in our environment, food as well as in baby food  
60 jars(Nougadère et al., 2020; Sánchez-Santed et al., 2016) . Recently, enhanced A $\beta$  aggregation,  
61 microgliosis and neuronal loss have been observed after treatment of AD transgenic mouse  
62 model with residual amounts (0.1  $\mu$ g/L in drinking water for 9 months) of a cocktail of 3  
63 fungicides, cyprodinil, mepanipyrim, and pyrimethanil (Lafon et al., 2020). A $\beta$  pro-aggregating  
64 activity appears to be mediated by the direct interaction of fungicides with A $\beta$ (1-42).  
65 Nevertheless, the influence of such chemical agents in A $\beta$ (1-42) assembly, and

66 amyloidogenesis, as well as their interplay with specific subsets of A $\beta$ (1-42) assemblies remain  
67 to be determined.

68 While the underlying molecular events occurring during A $\beta$ (1-42) fibril growth are now  
69 widely recognized, less is known about the transient oligomers formed at earlier stages  
70 especially during the lag phase. The reason is that conventional techniques do not provide  
71 sufficient resolution to detect and characterize these intermediate species in bulk assays.  
72 Therefore, an experimental technique is needed allowing for high-sensitive real-time detection  
73 and characterization of early stages of A $\beta$ (1-42) assembly. Recently, the use of nanopore  
74 technology demonstrated very promising results thanks to the possibility to obtain information  
75 about the protein aggregate population under continuous measurement (Houghtaling et al.,  
76 2018b). Biological nanopores were widely used for protein sensing. They were shown to be  
77 able to detect minor differences in peptide sequences (Asandei et al., 2017; Huang et al., 2019;  
78 Ouldali et al., 2020; Piguet et al.) and to analyse the protein folding/unfolding process (Di  
79 Marino et al., 2015; Merstorf et al., 2012; Oukhaled et al., 2007; Rodriguez-Larrea and Bayley,  
80 2013). They were used to investigate the prion protein and  $\alpha$ -synuclein misfolding (Madampage  
81 et al., 2012; Stefureac et al., 2008; Tavassoly and Lee, 2012), A $\beta$  peptide aggregation (Bonome  
82 et al., 2019; Wang et al., 2011) or binding with metal ion (Asandei et al., 2013; Asandei et al.,  
83 2014). The A $\beta$ (1-42) aggregation was evidenced by  $\alpha$ -hemolysin as bumping event, making it  
84 impossible to obtain information about the amyloid size (Wang et al., 2011). The solid-state  
85 nanopores have advantages of robustness, reusability and scalable diameter (Lepoitevin et al.,  
86 2017). They allow the characterization of conformational fluctuations of proteins (Waduge et  
87 al., 2017), their interactions with nanoparticles (Coglitore et al., 2018; Coglitore et al., 2019) as  
88 well as protein aggregation. The unmodified SiN nanopore allows detection of lysozyme  
89 oligomers (Balme et al., 2016). The glass nanopipettes are also used for amyloid detection as  
90 shown for lysozyme (Martyushenko et al., 2015),  $\alpha$ -synuclein (Chau et al., 2020) and A $\beta$ (1-42)

91 (Yu et al., 2019). However, the nanopore functionalization is required to prevent the nanopore  
92 fouling in the case of A $\beta$ (1-40) (Yusko et al., 2011) or  $\alpha$ -synuclein (Hu et al.), and to allow  
93 discrimination of oligomers (Yusko et al., 2012). The functionalization with PEG is efficient to  
94 discriminate different types of protein aggregates (Giamblanco et al., 2018b) while at the same  
95 time increasing the nanopore lifetime (Roman et al., 2017). The limitation of solid-state  
96 nanopores and glass nanopipettes is that they do not allow to differentiate aggregates and  
97 protofibrils larger than the nanopore diameter. Indeed, when the aggregates are larger than the  
98 pore, only bumping events are observed making the size discrimination impossible. To  
99 overcome this problem, our group proposed the use of conical track-etched nanopore  
100 (Giamblanco et al., 2018a). The latter are more used for their ionic-diode properties than single  
101 molecule sensing (Ma et al., 2020; Zhao et al., 2017). However, by combining this geometry  
102 and a very long lifetime, they are more convenient to monitor protein aggregation kinetic  
103 (Giamblanco et al., 2018a; Giamblanco et al., 2020a) as well as their enzymatic degradation  
104 (Giamblanco et al., 2020b).

105 To investigate the influence of extrinsic factors on A $\beta$ (1-42) assembly we selected the  
106 fungicide pyrimethanil, which belongs to the anilinopyrimidine class. In this work, the A $\beta$ (1-  
107 42) amyloidogenesis in the absence and presence of pyrimethanil was monitored by a thioflavin  
108 T (ThT) binding assay, and characterized using conical track-etched nanopore technology as an  
109 *ex-situ* assay. Using this up-to-date approach, we focused mainly on the lag phase that was  
110 determined during the amyloid fibril formation. To do so, we produced several nanopores with  
111 a tip diameter adapted to the degree of aggregate maturation, and analysed the A $\beta$ (1-42) species  
112 present from a reaction mixture at different times using resistive pulse experiments. The  
113 experimental data of current blockades were compared with a theoretical model and with the  
114 results of molecular dynamics simulations.

## 115 **2. Materials and methods**

116 **2.1. A $\beta$ (1-42) aggregation and characterization**

117 ***Preparation of monomeric A $\beta$ (1-42)***. A $\beta$ (1-42) peptides (ERI Amyloid Laboratory LLC,  
118 Oxford, CT,USA)) were maintained in a monomeric state using the protocol described in Serra-  
119 Batiste et al. (Serra-Batiste et al., 2016). Briefly, A $\beta$ (1-42) peptides were dissolved in a 6.8 M  
120 guanidine thiocyanate solution (Sigma-Aldrich) at a concentration of 8.5 mg mL<sup>-1</sup>. The solution  
121 was then sonicated for 5 min at 52 °C, and diluted with ultrapure water to reach a final  
122 concentration of 5 mg mL<sup>-1</sup> of A $\beta$ (1-42) peptides and 4 M of guanidine thiocyanate. Solution  
123 was centrifuged at 10,000 g for 6 min at 4°C. The collected supernatant was filtered (PVDF,  
124 0.45  $\mu$ m) and then injected into a Superdex 75 Increase 10/300GL column (GE Healthcare Life  
125 Science) previously equilibrated with 10 mM sodium phosphate buffer pH 7.4. Purification was  
126 performed with a 0.5 mL min<sup>-1</sup> flow to collect the peak attributed to monomeric A $\beta$ (1-42). The  
127 A $\beta$ (1-42) peptides concentration was determined with a NanoDrop 8000 spectrophotometer  
128 (Thermo Scientific). The aliquots of peptides were stored at -20 °C.

129 ***Preparation and characterization of A $\beta$ (1-42) aggregates***. A $\beta$ (1-42) stock solution was  
130 diluted to 30  $\mu$ M in a 10 mM sodium phosphate buffer, pH 7.4 and left to aggregate in low-  
131 binding Eppendorf tubes for a final volume of 600  $\mu$ L. Experiments with pyrimethanil were  
132 conducted under the same conditions, except that fungicide was added from a filtered (PVDF,  
133 0.22  $\mu$ m) stock solution to get a 1:15 molar ratio (A $\beta$ (1-42): pesticide), with a final  
134 concentration of DMSO of 1% (v/v). To keep the identical conditions, an equal volume of  
135 DMSO was added to the control tube. Tubes were arranged vertically and incubated at 25 °C  
136 under quiescent state. The fibril formation was monitored by a thioflavin T (ThT) binding assay.  
137 Briefly, 20  $\mu$ L aliquots were withdrawn at specific times and mixed with 14  $\mu$ L of 142 mM  
138 GlyNaOH buffer, pH 8.3 and 6  $\mu$ L of 100  $\mu$ M of ThT in a 96-well plate of black polystyrene  
139 with a clear bottom coated with a PEG (Thermofisher Scientific). ThT fluorescence of each  
140 sample was measured ( $\lambda_{ex}$  = 445 nm and  $\lambda_{em}$  = 485 nm) in a Fluoroskan Ascent microplate

141 fluorimeter (Thermofisher Scientific). Aggregation profiles were generated with GraphPad  
142 Prism software. Curves were fitted using the built-in sigmoidal fit. Each kinetic trace was fitted  
143 independently to extract the time required to reach 50% of the maximum fluorescence intensity,  
144 known as  $t_{50}$ .

## 145 **2.2. Nanopore production and characterization**

146 Single tracks were produced by Xe irradiation ( $8.98 \text{ MeV u}^{-1}$ ) of PET film ( $6 \mu\text{m}$ ,  
147 Goodfellow) at GANIL (SME line, Caen, France). The activation of the track was performed  
148 by a UV exposition of 8 h for the tip side and 11 h for the base side (Fisher bioblock;  
149 VL215.MC,  $\lambda=312 \text{ nm}$ ) before the chemical etching process. The etching of the conical  
150 nanopore was performed under asymmetric conditions as previously reported (Lepoitevin et al.,  
151 2016). After the nanopore etching, the film was stabilized overnight in  $18 \text{ M}\Omega$  water. The  
152 approximate tip diameter was obtained by conductance measurement. After the chemical  
153 etching, the current-voltage (I-V) curve was measured at pH 7. Then the nanopore was  
154 functionalized with  $\text{PEG}_{5k}\text{-NH}_2$  (Nanocs, PG1-AM-5K) using 1-ethyl-3-(3-  
155 dimethylaminopropyl) carbodiimide hydrochloride (EDC, Sigma Aldrich, E7750) as  
156 previously reported in order to prevent the unspecific adsorption and improve the  
157 nanopore lifetime<sup>35</sup>. The success of the grafting was confirmed by the decrease of I-V curve  
158 slope due to the replacement of  $\text{COO}^-$  by the PEG which diminished the diameter of the  
159 nanopore (see figure S1). The estimation of nanopore size was performed using quasi-1D model  
160 (see supporting information section 1)

## 161 **2.3. Detection of $\text{A}\beta(1-42)$ aggregates using resistive pulse**

162 The nanopore functionalized with PEG moieties was mounted between two compartments of  
163 a Teflon cells filled with PBS 1X aqueous solution (pH = 7.2). The  $\text{A}\beta(1-42)$  at different  
164 aggregation times (from 0 to 72 h) in presence or not of pyrimethanil was added to the base side  
165 to reach a concentration of 30 nM (monomer equivalent). The resistive pulse experiments were



166 performed using a patch-clamp amplifier (EPC 10, HEKA electronics, Germany) with Ag/AgCl  
167 electrodes. A voltage of 1 V was applied to the working electrode located in the tip side  
168 compartment to drive the negatively charged A $\beta$ (1-42), (isoelectric point of 5.5) to pass through  
169 the nanopore from the base to the tip side. The ionic currents were recorded at 50 kHz. The  
170 signal was filtered at 5 kHz by a Bessel filter. The resistive pulse detection was recorded on the  
171 fly. The current traces were further analysed to detect events using lab-made software “Peak  
172 Nano Tools” developed using Labview. First the signal was filtered using Butterworth filter  
173 1 kHz order 1. The threshold for the event detection was defined as follows: (i) correct the  
174 baseline using a Stavinsky-Golay filter (ii), define the noise levels by the global standard  
175 deviation methods (iii) define the threshold. In this work, the threshold has been fixed at about  
176  $4\sigma$  (where  $\sigma$  is the standard deviation of the signal after baseline correction).

#### 177 **2.4. Molecular dynamic simulation**

178 *Description of the protocol* Classical all-atom MD simulations were performed using the  
179 NAMD.2.12 package(Phillips et al., 2005) . The different systems were solvated in a water box  
180 large enough to prevent the interaction between the central part (the conical pore) and its  
181 neighbouring periodic cells. KCl ions (at a concentration of 1 M) were added to the water  
182 (simulated using the TIP3P model) to reproduce the experimental environment. CHARMM36  
183 (Brooks et al., 2009; Lee et al., 2015) force-field optimization parameters were used in all  
184 simulations. During the simulations, the system temperature and pressure were kept constant at  
185 300 K (Langevin dynamics) and 1 atm (Langevin piston), respectively. The long-range  
186 electrostatic forces were evaluated using the classical particle mesh Ewald (PME) method with  
187 a grid spacing of 1.2 Å, and a fourth-order spline interpolation. The integration time step was  
188 equal to 1 fs. Each simulation employed periodic boundary conditions in the three directions of  
189 space.

190 *Description of the conical nanopore.* To build the conical solid-state nanopore ( $R_{tip} = 3$  nm,  
191  $R_{base} = 3.5$  nm, length=14.8 nm) several carbon nanotube sections of different radii were  
192 associated and centred along the nanopore axis. To model the chemical structure of PET  
193 nanopore used in the experiments, one third of the carbon atoms constituting the nanopore were  
194 randomly configured as oxygen atoms. Partial charges, positive for carbon and negative for  
195 oxygen atoms, were added while global neutrality of the nanopore was conserved. Each section  
196 was then modified according to the experimental functionalization of the conical nanopore by  
197 grafting 30 hydroxyls functions (0.10 M) to randomly picked carbon atoms. Then, three  
198 PEG 5K were added (1.15 M), as in the experiments. To place the PEG, a position of linkage  
199 was chosen with a random generator number. Nevertheless, to orient each molecule, we took  
200 into account the position of each one in order to avoid the superposition of the different  
201 structures. Finally, the functionalized nanopore was placed between 2 reservoirs of dimensions  
202 equal to  $133 \times 133 \times 68$  Å<sup>3</sup> and solvated with K<sup>+</sup> and Cl<sup>-</sup> ions concentration equal to 1 M. The  
203 reservoir size was chosen to be around twice the size of the conical-tube part of the nanopore.  
204 The complete system dimensions are  $133 \times 133 \times 285$  Å<sup>3</sup>, for a total of around 320.000 atoms,  
205 detailed as such: 24.000 for the nanopore, 2.400 for PEGs, 3.700 for ions and 290.000 for water.  
206 Once the complete functionalized system was obtained, it was optimized following three  
207 successive procedures. First, we minimized the energy of the total system at 0 K. Then, the  
208 system was progressively heated until reaching a temperature equal to 300 K. Finally, the  
209 system was left to evolve at the NPT ensemble, and physical observables were calculated using  
210 time averages. During all simulations, every atom constituting the conical nanopore was kept  
211 fixed. This system was relaxed for 30 ns, allowing for PEG to relax around the surface of the  
212 nanopore. For further computations dealing with ionic current calculations, various electric  
213 fields were applied. Those simulations were performed in the NVT ensemble. Once run, the  
214 determination of the ionic current was performed according to the procedure described in Ref

215 (Aksimentiev and Schulten, 2005) by following each ion in the nanopore during its  
216 displacement.

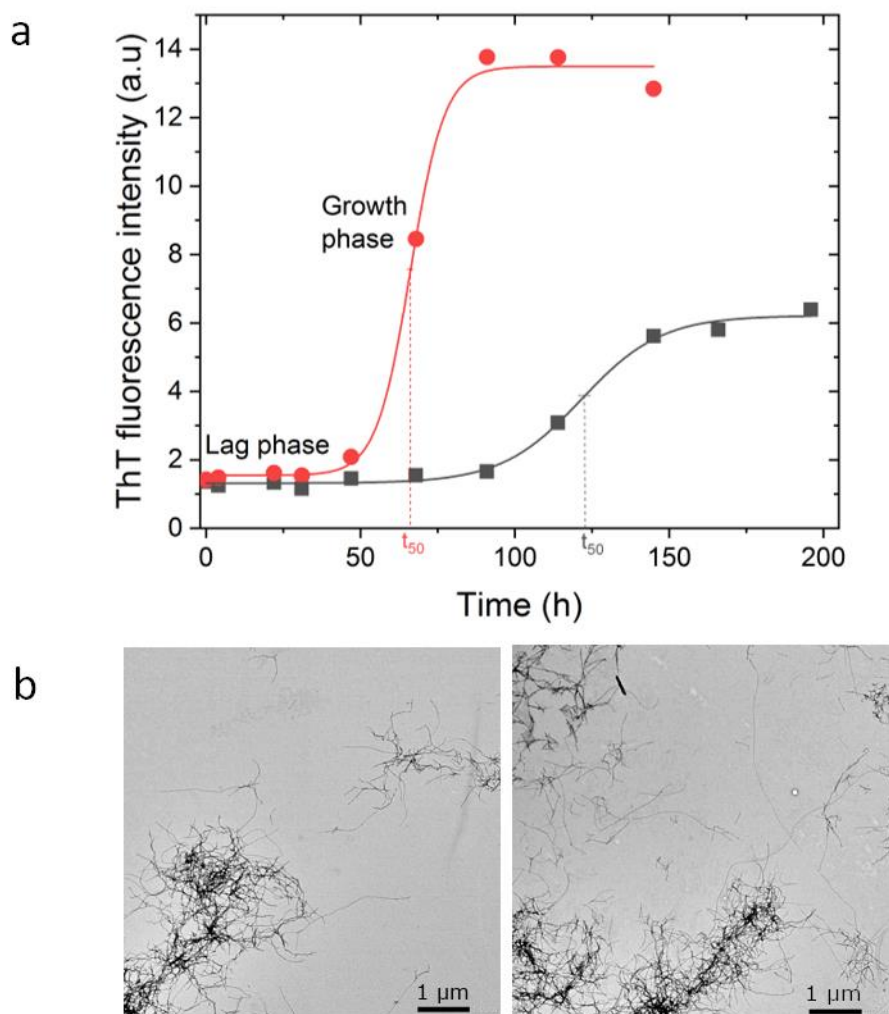
217 *Description of the simulated different amyloids. 5OQV/2NAO/2BEG:* Three types of A $\beta$ (1-  
218 42) amyloid arrangements were generated and studied by simulations. To the previously  
219 described 5OQV(Gremer et al., 2017) and 2NAO(Wälti et al., 2016)dual subunit amyloid  
220 structure, we also studied a single subunit (PDB id = 2BEG(Lührs et al., 2005) ) in order to see  
221 its role on the current perturbation inside the nanopore. First, we were interested in the  
222 behaviour of small amyloid structures (i.e., 2BEG) in the conical nanopore. Structures used in  
223 this case were extracted from RCSB Protein Databank, relaxed in water and 1M KCl ions for  
224 10 ns and then inserted inside the relaxed functionalized nanopore. Once it was shown that  
225 simulating translocation under a voltage was possible, we simulated the translocation of the  
226 bigger amyloid structures (2NAO and 5OQV). For each simulation run, the relaxed 2NAO or  
227 5OQV was placed at the entrance of the previously described functionalized nanopore, free of  
228 water and ions. Water and ions were then added into the systems and relaxed. Note that for the  
229 relaxed 2BEG amyloid, we started the simulation with the amyloid inside the nanopore.

### 230 **3. Result and discussion**

#### 231 **3.1. Impact of pyrimethanil on the aggregation**

232 The aggregation kinetics starting from pure monomeric A $\beta$ (1-42) was characterized by using  
233 the reporter dye thioflavin T, which undergoes an enhancement of quantum yield when bound  
234 to  $\beta$ -sheet structure of fibrils (Figure 1A). The addition of pyrimethanil efficiently accelerated  
235 the reaction by decreasing to 50% the half-time of aggregation ( $t_{50}$ ) (from about 122 to 66  
236 hours). The fluorescence intensity of ThT at the post-transition plateau in the presence of  
237 pyrimethanil was significantly higher (about a two-fold increase), compared to that obtained  
238 using A $\beta$ (1-42) fibrils alone. This supports the idea that pyrimethanil facilitates a  
239 conformational rearrangement leading to different fibril morphotypes. However, no major

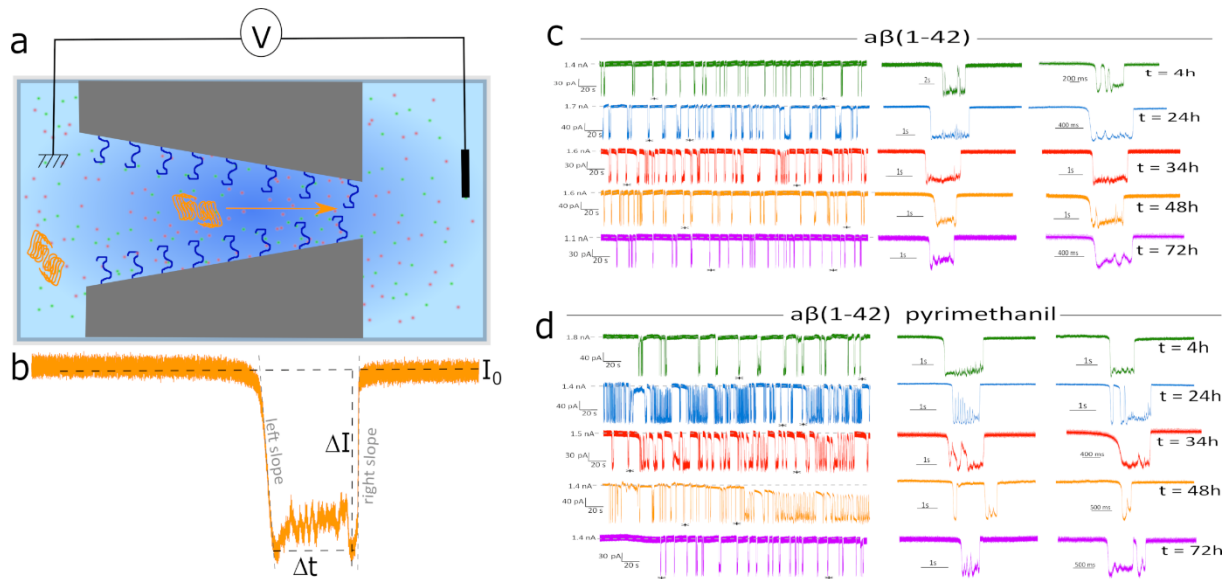
240 macrostructural changes induced by pyrimethanil treatment were revealed by transmission  
241 electron microscopy (Figure 1b-c).



242  
243 **Figure 1: Effect of pyrimethanil on the kinetics of Aβ fibrils formation. (a) Aβ(1-42) monomers (30 μM)**  
244 **were incubated with pyrimethanil (750 μM) (red curve), or with an equivalent volume of DMSO (1%) (black**  
245 **curve) with a ratio 1:15. ThT fluorescence intensity was measured once a day (a.u., arbitrary units). The**  
246 **different values obtained were plotted. The sigmoidal fits were done using Boltzmann equation ( $I = I_0 +$**   
247  **$(I_0 - I_F)/1 + \exp(t_{50} - t/a)$ ) where I,  $I_0$  and  $I_F$  are the fluorescence intensity at time t, at the initial and**  
248 **final plateaus respectively, and  $t_{50}$  the half-time of aggregation. (b) Negative-stained transmission electron**  
249 **micrographs of Aβ(1-42) fibrils formed in the absence (left panel) or presence (right panel) of pyrimethanil.**

### 250 3.2. Investigation of the lag phase using nanopore

251 To further characterize the pro-aggregating effect of pyrimethanil on A $\beta$ (1-42) during the lag  
252 phase of amyloidogenesis the aliquots were withdrawn at different time intervals and analysed  
253 using conical track-etched nanopores. To do so, we used a conical nanopore functionalized with  
254 PEG as previously reported(Giamblanco et al., 2018a). The characterization of nanopore using  
255 quasi-1D model for pore resistance gives a pore tip radius  $r_t \sim 4.7$  nm while the pore base  
256 radius  $r_b = 170$  nm was determined by SEM (See Supplementary Information S1). The detection  
257 of A $\beta$ (1-42) aggregates was performed using resistive pulse methods from the base to the tip  
258 side (Figure 2a). From the current traces, we detected events characterized by the relative  
259 current blockade noted  $\Delta I/I_0$ , the dwell time  $\Delta t$ , both the left and right slope and the variance of  
260 the close current (Figure 2b). In Figure 2, the current trace recorded for A $\beta$ (1-42) at various  
261 incubation times (from 4 h to 72 h) with pyrimethanil or not are reported. First, we observed  
262 the current blockade for all the samples. This means that after 4h in presence or absence of  
263 pyrimethanil, A $\beta$ (1-42) aggregates are detected. The zoom of certain current blockades reveals  
264 large fluctuations of the closed current levels that can be assigned to the reorientation of an  
265 aggregate inside the detection zone of the nanopore. During the experiment, we also observe  
266 events where the base line level is not reached while the event is supposed to be finished (see  
267 figure 2 d, orange line). This could have two interpretations (i) an aggregate is adsorbed close  
268 to the narrow aperture or (ii) a large aggregate is trapped inside the nanopore. Because the origin  
269 of such events is not clear, we did not consider these events in the further analysis. For each  
270 event, we analysed both the left and the right slope (see SI-2, figure S3). For all recorded events,  
271 the values of the left slope corresponding to the beginning of the event are one order of  
272 magnitude larger than the right one that corresponds to the aggregate exit from the nanopore.  
273 Such dissymmetry is a typical feature of the track-etched nanopore presenting a conical shape.



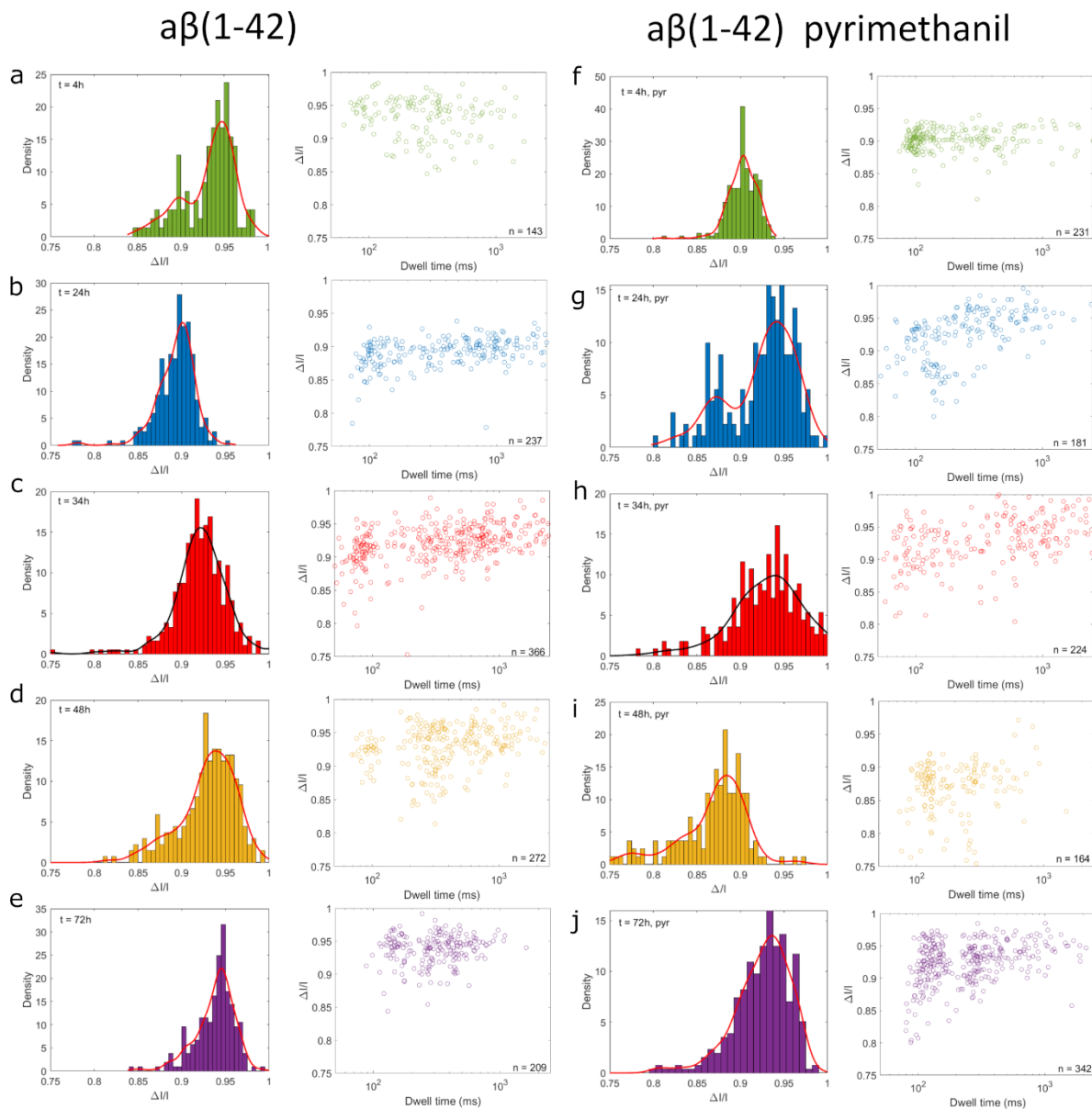
274

275 **Figure 2: (a) Sketch of nanopore experiments. A $\beta$ (1-42) after incubation 72 h with and without pyrimethanil**  
 276 **(b) illustration of the parameters measured for each current blockade. Examples of current traces recorded**  
 277 **during resistive pulse experiments for A $\beta$ (1-42) after incubation without (c) and with pyrimethanil (d) for**  
 278 **various times. The experiments were performed using nanopore  $r_t \approx 4.7$  nm. On the right side, example of**  
 279 **current blockade is reported.**

280 From the current traces, we detected events characterized by the relative current blockade  
 281 noted  $\Delta I/I_0$  and the dwell time  $\Delta t$ . In Figure 3, both the distribution of  $\Delta I/I_0$  and the event map  
 282 recorded for A $\beta$ (1-42) after 4 h, 24 h, 34 h, 48 h, 72 h, incubation without or with pyrimethanil  
 283 are reported. Without pyrimethanil and after 4h, the distribution is bimodal centred to 0.90 and  
 284  $0.94 \pm 0.04$  evidencing the presence of two distinct populations in the sample. After 24h, the  
 285 distribution becomes monomodal centred to  $0.90 \pm 0.04$ . Interestingly, the larger  $\Delta I/I_0$   
 286 distribution disappears. This result is counter-intuitive. Indeed, we expected that with time the  
 287 aggregate should be larger. However, we observe an increase of the dwell time distribution  
 288 (Figure SI-5). This means that the assemblies occupy less space inside the nanopore but  
 289 translocate more slowly. This suggests at this stage a reorganization of the aggregate. After 34h  
 290 and 48h, we observe that the amplitude of the relative current blockade increases and their  
 291 distribution is wider ( $0.92 \pm 0.06$  and  $0.93 \pm 0.06$  respectively). In addition, the distribution of the

292 dwell time is more spread and reveal two clusters. The first population exhibits a dwell time >  
293 105 ms, while the second one is spread from 110 ms to 2500 ms. This suggests that the  
294 population of oligomers is more and more heterogeneous. After 72 h, the  $\Delta I/I_0$  distribution is  
295 shaper, reaching  $0.95 \pm 0.04$ . On the other hand, the dwell time distribution is also more compact  
296 since only one population is obtained. Concerning the distribution of  $\Delta I/I_0$  and the events map  
297 for the for A $\beta$ (1-42) incubated in presence of pyrimethanyl we can report that after 4 h of  
298 incubation, the distribution of  $\Delta I/I_0$  is centred to  $0.90 \pm 0.04$ . After 24 h and 34 h, the distributions  
299  $\Delta I/I_0$  are wider and centred  $0.94 \pm 0.06$  and  $0.94 \pm 0.09$ . We also observe that the dwell times  
300 distributions are more spread, suggesting heterogeneity in the sample. However, compared to  
301 the sample without pyrimethanyl, the presence of two distinct populations of dwelling time is  
302 not evidenced. After 48 h, the distribution centre of  $\Delta I/I_0$  decreases to  $0.88 \pm 0.06$ . On the other  
303 hand, the dwell time distribution is centred to lower values. This clearly evidences the presence  
304 of smaller assemblies. It is interesting to notice that 48 h corresponds to the beginning of the  
305 growth phase (figure 1a) determined by the ThT test. After 72 h, the aggregation process is  
306 clearly under the growth phase, the distribution shifts toward larger value of  $\Delta I/I_0$  ( $0.93 \pm 0.07$ )  
307 and longer dwell time. Our nanopore experiments reveal that the evolution of the population of  
308 A $\beta$ (1-42) follows two different trends. Without the pyrimethanyl, after the reorganization  
309 occurring between 4 h and 24 h, the A $\beta$ (1-42) aggregates are more and more polydispersed with  
310 the incubation time. This is also the case for the sample incubated with pyrimethanyl before the  
311 starting of the growth phase where the aggregate structures become more ordered adopting a  $\beta$ -  
312 sheet organization. After 48 h of incubation with pyrimethanyl, the presence of smaller  
313 assemblies revealed by nanopore experiments is consistent with a quaternary structural  
314 convergence, by reducing the parental polydispersity, and generation of smaller assemblies.  
315 These results led us to conclude that conformational rearrangements and protomer exchanges,

316 i.e., dissociation/association events, take place within the initial heterogeneous population of  
 317 assemblies(Dear et al., 2020b; Dear et al., 2020a; Michaels et al., 2020).



318  
 319 **Figure 3: histograms of relative current blockade without (a-e) and with pyrimethanil (f-j) and**  
 320 **corresponding event maps of current blockade parameters induced by Aβ(1-42) after various incubation**  
 321 **time (4 h green, 24 h blue, 34 h red, 48 h orange, 72 h violet), the lines are the fit using nonparametric law**  
 322 **to evaluate the centre of the distribution. The experiments were performed using nanopore  $r_t = 4.7$  nm.**

323 We then performed a theoretical analysis of the expected blockade to estimate the size of  
 324 Aβ(1-42) aggregate. In general, the current blockade induced by a particle dwelling into a  
 325 nanopore depends on the particle size, shape, position, orientation, surface charge and



326 electrolyte solution (Houghtaling et al., 2018a). In nanofluidic systems, different  
327 theoretical/computational techniques are commonly used to describe the current blockade and  
328 the translocation process (Chinappi and Cecconi, 2018; Qiu et al., 2016). Here, we start our  
329 analysis using a theoretical model while in the next section, we discuss molecular dynamics  
330 simulations.

331 One evidence shown in Fig 2 is that the current blockades are always relatively high, i.e.  
332  $\Delta I/I_0 \simeq 0.85 - 0.95$ . Two questions naturally arise, i) what is the shape of the amyloid  
333 aggregates responsible for such high blockades? and ii) why, despite the expected  
334 polydispersity of the sample (in a growing process, we expect that different populations, from  
335 monomers to large aggregates are present simultaneously) small blockades (e.g.,  $\Delta I/I_0 > 0.7$ )  
336 are not observed?

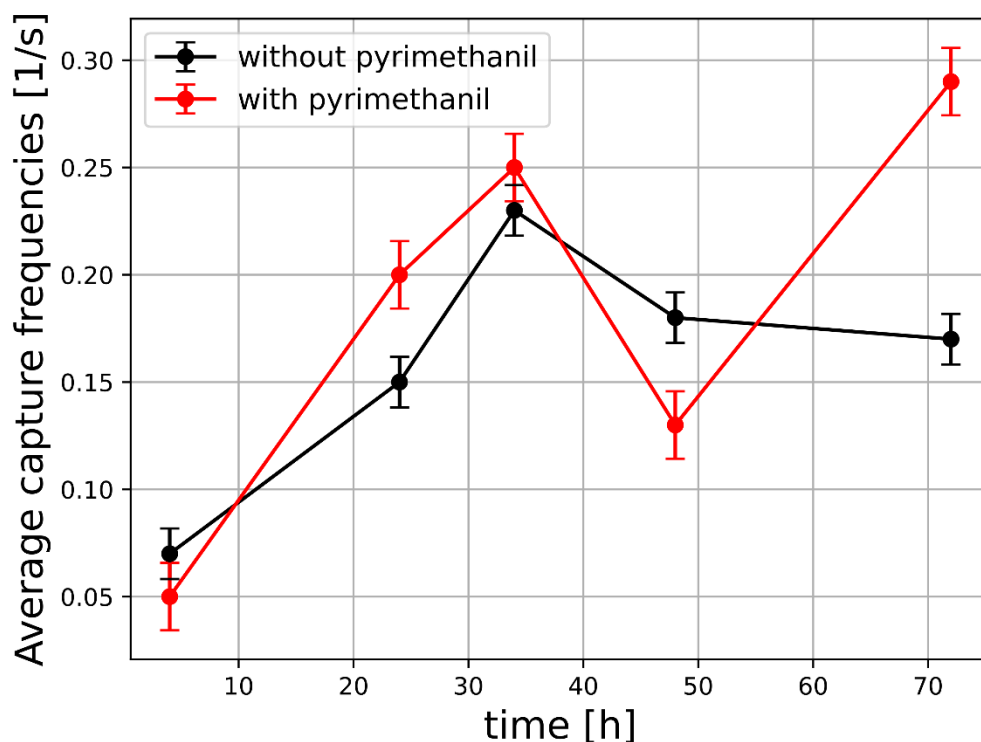
337 To answer to these questions we employed a quasi-1D model that allows estimating current  
338 blockades associated with the presence of a particle partially blocking the pore (DeBlois and  
339 Bean, 1970; Di Muccio et al., 2019; Giambianco et al., 2018a). Assuming that the aggregates  
340 have a spherical shape with radius  $r_a$ , our model predicts that the blockade ( $\Delta I/I_0 \simeq 0.85 -$   
341  $0.95$ ) are due to aggregate radii close to the nanopore tip radius, i.e.  $r_a \simeq r_t$ , see section 3 of SI  
342 for details on the physical model. This answers to the first question: the experimentally  
343 observed blockades correspond to particles of radius  $r_a > 4.5$  nm that occupies the pore tip.  
344 The present model is developed for spheres, similar analytic results can be obtained for other  
345 simple shapes (e.g. short cylinders or ellipses). The different peaks observed experimentally  
346 (see e.g. figure 2a or figure 2g) can be ascribed to particles with slightly different shape and size.

347 Moreover our model predicts that amyloid aggregates with smaller radius would result in  
348 much smaller blockades, e.g., an aggregate of radius 4 nm would gives  $\Delta I/I_0 \simeq 0.2$ . In  
349 principle, such blockade should be detected by our nanopore sensing system. Hence, the fact  
350 that such small blockades are not observed deserve an additional explanation. In our opinion,

351 the most reasonable explanation is that such small aggregates exist in the solution and they  
352 actually translocate through the pore. However their translocation is so fast that the signal is not  
353 recorded. To support this interpretation, we estimate the dwell time of an aggregate as a function  
354 of its radius, see section S4 of SI. The dwell time predicted using only electrophoresis as driving  
355 force is much smaller than the observed one. This implies that aggregates are further slowed  
356 down by interaction with the pore wall. This interaction is effective only for aggregate of the  
357 same size of the pore tip. In summary, our model suggests the following interpretation:  
358 aggregates of different sizes are present in the solution. The ones are smaller than the pore tip,  
359  $r_a < r_t$ , translocate too fast to be detected. The ones have a size similar to the pore,  $r_a \sim r_t$ , are  
360 slowed down by the interaction with pore tip wall and they provide an almost complete blocking  
361 of the current  $\Delta I/I_0 > 0.85$ . Larger aggregates,  $r_a > r_t$ , could exist in the solution and the  
362 resulting blockage would be even larger. Nevertheless, the analysis of the left and right slopes  
363 of the blockade events suggest that all the events are associated to translocations (see Figure 2  
364 and Fig S2). Consequently, larger aggregates probably bump at the pore surfaces without  
365 reaching the sensing region.

366 In the light of this interpretation, the pore can also be used as a counter for aggregate of size  
367  $r_a \approx r_t$ . The event frequency is reported in Figure 4. In the lag phase  $t < 40$ h, the event  
368 frequency increases with time as expected in an aggregation process. This increase is slightly  
369 more pronounced in the experiments with pyrimethanil, suggesting a possible positive effect of  
370 pyrimethanil in the first phase of aggregation, coherently with the fluorescence data in Figure  
371 1. With pyrimethanyl, we observe a decrease of the capture rate at 48 h of incubation. This can  
372 be explained by a decrease of the aggregate size and thus a part of these aggregates would  
373 become too small to be detected by nanopore. Interestingly, the evolution of the capture rate  
374 and the size of aggregate suggest that the pyrimethanyl induce a mechanism of aggregation in  
375 two steps due to a reorganization and/or fragmentation phenomena.

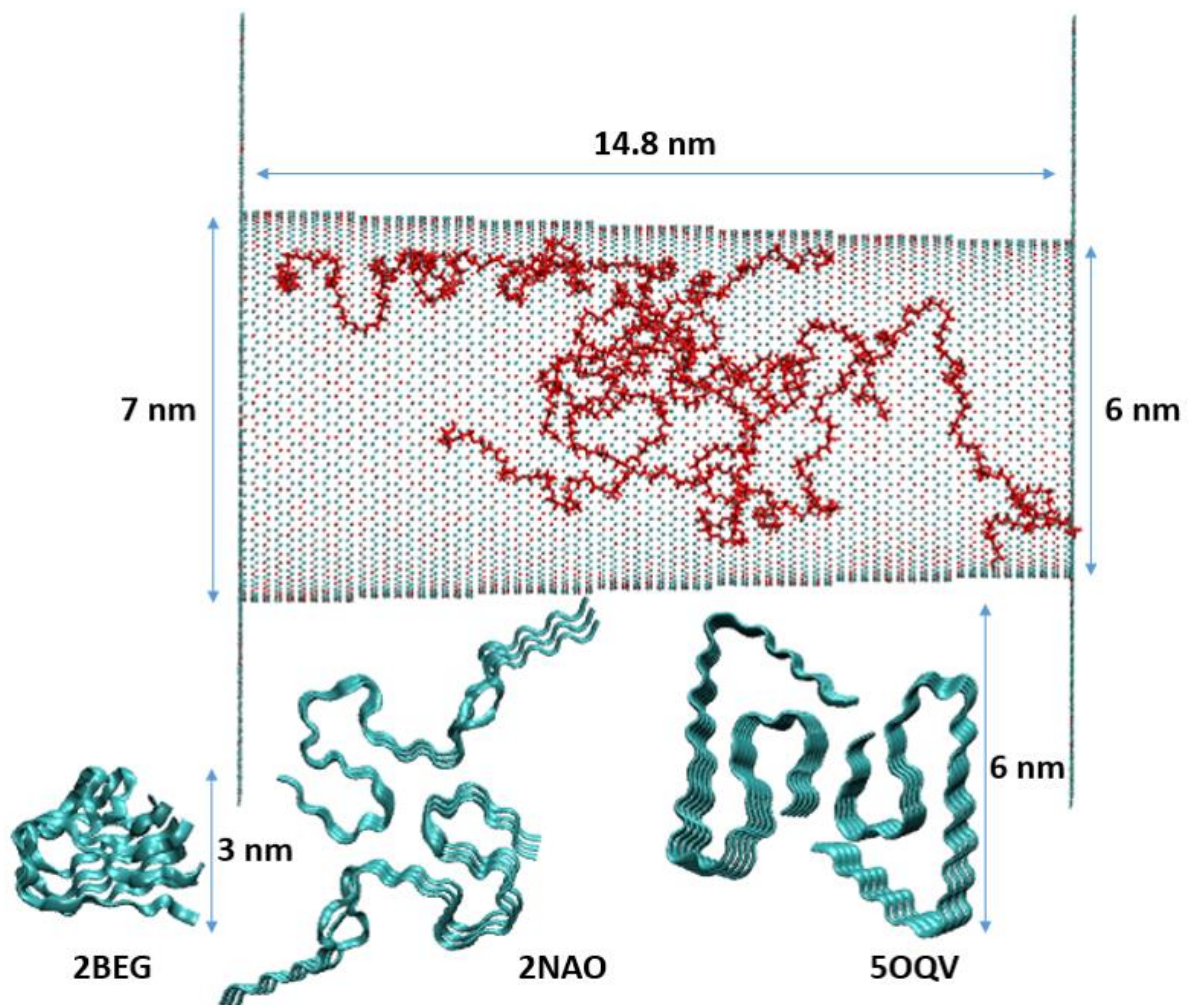
376 At this stage, several questions are still open to draw a complete description of the current  
377 blockade. Indeed, we found that the dwell time is long (until second scale) and the origin of the  
378 fluctuation occurring during the aggregate translocation is not fully understood. We plot in  
379 Fig. S4 the relation between the standard deviation of the current blockade vs the dwell time  
380 for each event. First, we can observe that the dispersion of the standard deviation increases with  
381 the dwell time evidencing that the fluctuation occurs more often during the long event. Second,  
382 the disparity of the standard deviation seems dependent on the incubation time and the presence  
383 of pyrimethanil. Typically, for the sample incubated without pyrimethanil, it is narrow after  
384 72 h incubation while in presence of pyrimethanil, it becomes narrow after 48 h. The latter  
385 could be concomitant with the apparition of ordered  $\beta$ -sheet structure. This is in accordance  
386 with a mechanism of aggregation in two steps suggested by the evolution capture rate and the  
387  $\Delta I/I_0$ .



388  
389 **Figure 4: Average capture frequency for each experiment with (red curve) and without (black curve)**  
390 **pyrimethanil.**

391 **3.3. Molecular dynamic simulation**

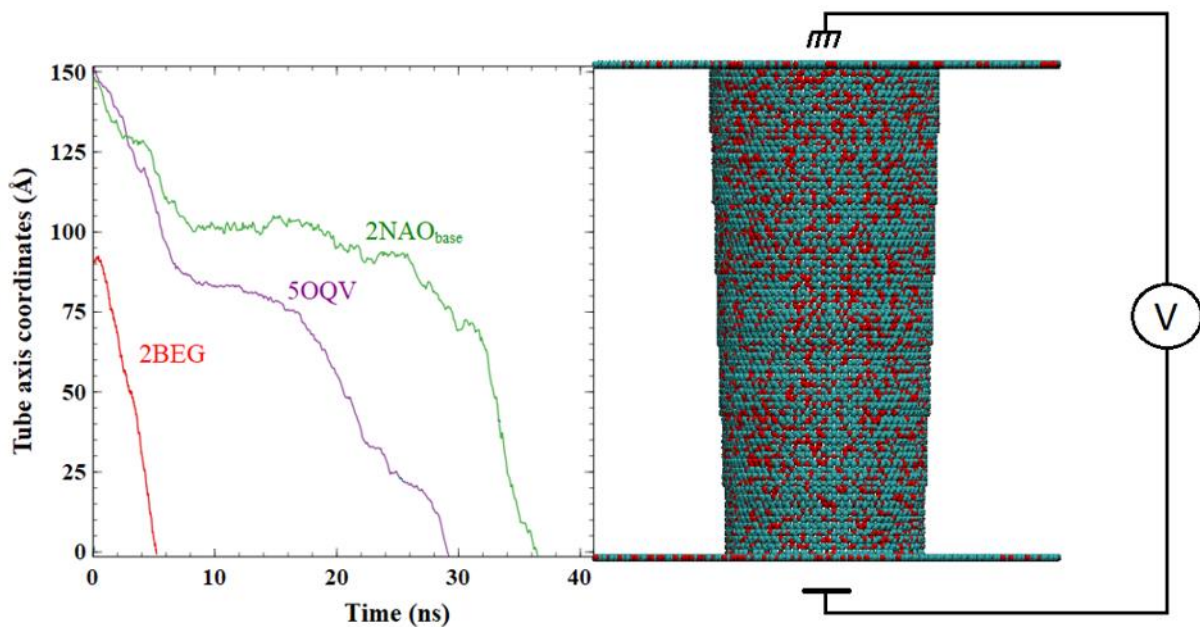
392 To provide additional insights on the A $\beta$ (1-42) aggregate translocation through the nanopore,  
393 we use molecular dynamic simulations. We aim to demonstrate that the interaction between the  
394 nanopore and the aggregate is strongly depending on their structure. For this, we choose  
395 different A $\beta$ (1-42) aggregates from the PBD even if they are not strictly identical to the  
396 experimental one. First, we studied the interaction between the nanopore and the A $\beta$ (1-42)  
397 aggregate with a single subunit structure (PDB-id 2BEG) (see Supplementary Information S5  
398 and Video\_S1), before generalizing this approach to the larger systems (2NAO and 5OQV PDB  
399 structures, respectively) (Fig. 5). We notice that the nanopore is smaller than the experimental  
400 one ( $r_t = 3$  nm while  $r_t = 4.7$ ) to keep a reasonable simulation box.



401

402 **Figure 5. Snapshots of different elements of the simulations at full scale. Top: functionalized nanopore.**  
403 **Bottom from left to right: 2BEG, 2NAO and 50QV fibrils in ribbon representation.**

404 The translocation of the different fibril structures in the nanopore was investigated for two  
405 voltages (0.2 V and 2 V, electric field oriented from tip to base). Under 0.2 V, we did not  
406 observe A $\beta$ (1-42) aggregate displacement (see Supplementary Information S5). Thus, we  
407 focused our studies at a higher voltage (2 V). The translocation does not exhibit a smooth and  
408 linear behaviour as shown in Figure 6. We note here that some of our attempts led to different  
409 phenomena than expected. Our attempt with 2NAO (see video\_S3) led to the protein adsorption  
410 on the nanopore. After  $\sim$ 11 ns of stability (plateau in Figure 6), the protein splits itself in two  
411 subunits with one resuming translocation while the other stays adsorbed. The 50QV protein  
412 did not adopt the same behaviour, since no splitting has been observed during its translocation  
413 (see video\_S4 and video\_S6). Note that these observations are, of course, heavily dependent on  
414 the entrance's radius and of the PEG conformation.



415

416

417 **Figure 6: Position of each protein's mass centre over the axis of the nanopore. The base entrance of the**  
418 **nanopore is positioned at coordinate 148.4 Å whereas tip entrance is situated at 0 Å.**

419 Once the translocation was achieved, we extracted from simulations the 1-D speed of each  
 420 mass centre of protein along the nanopore axis in order to compute the average speed and to  
 421 observe the different behaviours over the translocation (**Table 1**).

422 **Table 1: Translocation events of 5OQV, 2NAO and 2BEG in the different tested configurations. The**  
 423 **translocation duration and the average speed of the protein were obtained through the analysis of Figure 6.**  
 424 **Current blockades were computed using the analysis of the ions displacements.**

<b>Base entrance</b>	<b>Translocation Duration</b>	<b>Average speed</b>	<b>Number of monomer chains (sub-units)</b>
<b>5OQV</b>	27 ns	0.52 m s <sup>-1</sup>	9 (2)
<b>2NAO</b>	37 ns	0.41 m s <sup>-1</sup>	6 (2)
<b>2BEG</b>	4.6 ns	1.98 m s <sup>-1</sup>	5

425

426 When inserted from the base entrance, 5OQV and 2NAO translocation shows some sort of  
 427 similarity. Both proteins adsorb around the base of the nanopore, with less PEG coating on its  
 428 surface, for respectively ~8 and ~11 ns. Before and after the adsorption, we observe a quasi-  
 429 linear progression inside the nanopore. 5OQV enters faster in the base part than when it travels  
 430 through the tip part (speeds equal to 0.82 m s<sup>-1</sup> and 0.53 m s<sup>-1</sup> respectively, see Supplementary  
 431 Information S6). This can be explained by its difficulty to leave through the smaller tip radius,  
 432 its interaction with the PEG coating and the loss of its momentum while adsorbed. 2NAO shows  
 433 the opposite, with a speed of 0.58 m s<sup>-1</sup> in the base part and a speed equal to 0.81 m s<sup>-1</sup> in the  
 434 tip part. It has to be noted that the tip part speed is only for half the protein, as 2NAO splits  
 435 during the translocation. This resulted thus from possible interactions with the nanopore wall  
 436 and the PEG during the translocation of the proteins. Note that we also extracted the same

437 information for the previously described 2BEG system under a 2 V voltage which could be  
438 compared to other proteins. We can thus compare speed for the last ~8 nm, after all three  
439 proteins had been desorbed from the nanopore. For 5OQV (5643 atoms), half 2NAO (1881  
440 atoms) and 2BEG (1870 atoms), we obtain respective speeds of  $0.53 \text{ m s}^{-1}$ ,  $0.81 \text{ m s}^{-1}$  and  
441  $1.98 \text{ m s}^{-1}$ . These velocities at high-voltage lead to translocation times that are still smaller than  
442 experiments (27 ns, 37 ns and 4.6 ns, respectively).

443 Even if the molecular dynamic simulation was not performed under strictly the same  
444 condition as the experiments. The results allow providing elements to better understand the long  
445 dwell time. Indeed, as described in Supplementary Information, at low voltage (0.2 V), the  
446 interaction of the protein with the functionalized nanopore remained so high that no net  
447 displacement of the A $\beta$ (1-42) aggregate was observed. The adhesion of the protein, under the  
448 combined effect of a longer nanopore and a lower induced voltage, seems thus to have a crucial  
449 role in the amyloid dwell time as suggested by the different simulation conditions. In addition,  
450 the simulation highlights a slowdown of the A $\beta$ (1-42) aggregate when it reaches the PEG chain.  
451 Thus, it is plausible that similar scenario occurs inside conical nanopore, explaining long dwell  
452 time experimentally observed. According to theoretical conclusion, we could speculate that the  
453 small aggregate does not enter in interaction with the PEG and thus translocate faster (no event  
454 is observed), conversely the aggregate that reaches a critical size promoting a strong interaction  
455 with PEG is detected.

#### 456 **4. Conclusions**

457 Our work aimed to investigate the effect of pyrimethanil on A $\beta$ (1-42) aggregation. Using  
458 conical nanopores functionalized with PEG, we successfully detected A $\beta$ (1-42) aggregates at  
459 different time during the lag phase where the oligomer are often too small to be detected by  
460 other techniques. Regardless the incubation time and the presence of pyrimethanil, long large  
461 current ( $>0.7$ ) blockades are observed. Using an analytical model only based on geometrical

462 consideration, we could assign the detectable events to the A $\beta$ (1-42) aggregates with a size  
463 close to that of the sensing pore diameter. The molecular dynamic simulations confirm that the  
464 A $\beta$ (1-42) aggregates can translocate through the nanopore but interact with PEG explaining the  
465 long dwell time (hundreds ms scale) experimentally recorded. They also evidence amyloid/pore  
466 interaction in the zone without PEG coating confirming its importance. Such interaction let  
467 think splitting phenomena of the dimer structure occurs. The A $\beta$ (1-42) aggregates interaction  
468 with PEG and the uncoated zones will make the experimentalist to optimize the antifouling  
469 functionalization.

470 Generally speaking, by combining conventional techniques and single nanopore-based  
471 technology, our work confirms pyrimethanil as an enhancer of A $\beta$ (1-42) assembly during the  
472 lag phase of fibril formation. More interestingly, the nanopore approach evidences that the  
473 pyrimethanil induce an aggregation of A $\beta$ (1-42) mechanism in two steps including the  
474 reorganization after 48 h at the beginning of the elongation phase. This supports the emerging  
475 theory that the fibril formation involved numerous phases of dissociation, conversion and  
476 fragmentation. The original result here is that such phenomena can occur quickly in presence  
477 of pyrimethanil. This opens numerous questions about the health impact of certain chemicals  
478 used in agriculture.

## 479 **Acknowledgements**

480 This work was founded by Agence Nationale de la Recherche (ANR-19-CE42-0006,  
481 NanoOligo). MB, SB and MC acknowledge l'Università Italo Francese and Campus France  
482 through Galileo (project G16-173) and Vinci (project C3-1352) grants. Single tracks have been  
483 produced in GANIL (Caen, France) in the framework of an EMIR project. The authors thank  
484 E. Balanzat for the assistance at GANIL. Calculations were performed at the supercomputer  
485 regional facility Mesocentre of the University of Franche-Comté with the assistance of K.  
486 Mazouzi. This work was also granted access to the HPC resources of IDRIS, Jean Zay



487 supercomputer, under the allocation 2019 - DARI A0070711074 made by GENCI. Finally, part  
488 of this work was performed using computing resources of CRIANN (Normandy, France).

489

## 490 **References**

491 Aksimentiev, A., Schulten, K., 2005. Imaging  $\alpha$ -Hemolysin with Molecular Dynamics: Ionic  
492 Conductance, Osmotic Permeability, and the Electrostatic Potential Map. *Biophysical*  
493 *Journal*, 88(6), 3745-3761. *Biophysical journal* 88 (6), 3745–3761.  
494 doi:10.1529/biophysj.104.058727.

495 Asandei, A., Iftemi, S., Mereuta, L., Schiopu, I., Luchian, T., 2014. Probing of Various  
496 Physiologically Relevant Metals–Amyloid- $\beta$  Peptide Interactions with a Lipid Membrane-  
497 Immobilized Protein Nanopore. *J Membrane Biol* 247 (6), 531. doi:10.1007/s00232-014-  
498 9667-7.

499 Asandei, A., Rossini, A.E., Chinappi, M., Park, Y., Luchian, T., 2017. Protein Nanopore-  
500 Based Discrimination between Selected Neutral Amino Acids from Polypeptides.  
501 *Langmuir* 33 (50), 14451–14459. doi:10.1021/acs.langmuir.7b03163.

502 Asandei, A., Schiopu, I., Iftemi, S., Mereuta, L., Luchian, T., 2013. Investigation of  $\text{Cu}^{2+}$   
503 binding to human and rat amyloid fragments  $\text{A}\beta$  (1-16) with a protein nanopore. *Langmuir*  
504 : the ACS journal of surfaces and colloids 29 (50), 15634–15642. doi:10.1021/la403915t.

505 Balme, S., Coulon, P.E., Lepoitevin, M., Charlot, B., Yandrapalli, N., Favard, C., Muriaux,  
506 D., Bechelany, M., Janot, J.-M., 2016. Influence of Adsorption on Proteins and Amyloid  
507 Detection by Silicon Nitride Nanopore. *Langmuir : the ACS journal of surfaces and*  
508 *colloids* 32 (35), 8916–8925. doi:10.1021/acs.langmuir.6b02048.

509 Bonome, E.L., Cecconi, F., Chinappi, M., 2019. Translocation intermediates of ubiquitin  
510 through an  $\alpha$ -hemolysin nanopore: implications for detection of post-translational  
511 modifications. *NANOSCALE* 11 (20), 9920–9930. doi:10.1039/c8nr10492a.

512 Brooks, B.R., Brooks III, C.L., Mackerell Jr, A.D., Nilsson, L., Petrella, R.J., Roux, B., Won,  
513 Y., Archontis, G., Bartels, C., Boresch, S., 2009. CHARMM: the biomolecular simulation  
514 program. *Journal of computational chemistry* 30 (10), 1545–1614.

515 Carulla, N., Zhou, M., Giralt, E., Robinson, C.V., Dobson, C.M., 2010. Structure and  
516 intermolecular dynamics of aggregates populated during amyloid fibril formation studied  
517 by hydrogen/deuterium exchange. *Accounts of chemical research* 43 (8), 1072–1079.  
518 doi:10.1021/ar9002784.

519 Chau, C.C., Radford, S.E., Hewitt, E.W., Actis, P., 2020. Macromolecular Crowding  
520 Enhances the Detection of DNA and Proteins by a Solid-State Nanopore. *Nano letters* 20  
521 (7), 5553–5561. doi:10.1021/acs.nanolett.0c02246.

522 Chinappi, M., Cecconi, F., 2018. Protein sequencing via nanopore based devices: a  
523 nanofluidics perspective. *Journal of Physics: Condensed Matter*, 30(20), 204002. *J. Phys.:*  
524 *Condens. Matter* 30 (20), 204002. doi:10.1088/1361-648X/aababe.

525 Chin-Chan, M., Navarro-Yepes, J., Quintanilla-Vega, B., 2015. Environmental pollutants as  
526 risk factors for neurodegenerative disorders: Alzheimer and Parkinson diseases. *Front.*  
527 *Cell. Neurosci.* 9, 124. doi:10.3389/fncel.2015.00124.

528 Chiti, F., Dobson, C.M., 2017. Protein Misfolding, Amyloid Formation, and Human Disease:  
529 A Summary of Progress Over the Last Decade. *Annual review of biochemistry* 86, 27–68.  
530 doi:10.1146/annurev-biochem-061516-045115.

531 Coglitore, D., Coulon, P.E., Janot, J.-M., Balme, S., 2019. Revealing the Nanoparticle-Protein  
532 Corona with a Solid-State Nanopore. *Materials (Basel, Switzerland)* 12 (21).  
533 doi:10.3390/ma12213524.

534 Coglitore, D., Giambianco, N., Kizalaité, A., Coulon, P.E., Charlot, B., Janot, J.-M., Balme,  
535 S., 2018. Unexpected Hard Protein Behavior of BSA on Gold Nanoparticle Caused by

536 Resveratrol. *Langmuir : the ACS journal of surfaces and colloids* 34 (30), 8866–8874.  
537 doi:10.1021/acs.langmuir.8b01365.

538 Dear, A.J., Meisl, G., Šarić, A., Michaels, T.C.T., Kjaergaard, M., Linse, S., Knowles, T.P.J.,  
539 2020a. Identification of on- and off-pathway oligomers in amyloid fibril formation.  
540 *CHEMICAL SCIENCE* 11 (24), 6236–6247. doi:10.1039/c9sc06501f.

541 Dear, A.J., Michaels, T.C.T., Meisl, G., Klenerman, D., Wu, S., Perrett, S., Linse, S., Dobson,  
542 C.M., Knowles, T.P.J., 2020b. Kinetic diversity of amyloid oligomers. *Proceedings of the*  
543 *National Academy of Sciences of the United States of America* 117 (22), 12087–12094.  
544 doi:10.1073/pnas.1922267117.

545 DeBlois, R.W., Bean, C.P., 1970. Counting and Sizing of Submicron Particles by the  
546 Resistive Pulse Technique. *Review of Scientific Instruments* 41 (7), 909–916.  
547 doi:10.1063/1.1684724.

548 Di Marino, D., Bonome, E.L., Tramontano, A., Chinappi, M., 2015. All-Atom Molecular  
549 Dynamics Simulation of Protein Translocation through an  $\alpha$ -Hemolysin Nanopore. *The*  
550 *Journal of Physical Chemistry Letters*, 6(15), 2963-2968. *The Journal of Physical*  
551 *Chemistry Letters* 6 (15), 2963–2968. doi:10.1021/acs.jpcclett.5b01077.

552 Di Muccio, G., Rossini, A.E., Di Marino, D., Zollo, G., Chinappi, M., 2019. Insights into  
553 protein sequencing with an  $\alpha$ -Hemolysin nanopore by atomistic simulations. *Sci Rep* 9 (1),  
554 6440. doi:10.1038/s41598-019-42867-7.

555 Gazit, E., 2002. The "Correctly Folded" state of proteins: is it a metastable state? *Angewandte*  
556 *Chemie (International ed. in English)* 41 (2), 257–259. doi:10.1002/1521-  
557 3773(20020118)41:2<257:aid-anie257>3.0.co;2-m.

558 Giamblanco, N., Coglitore, D., Gubbiotti, A., Ma, T., Balanzat, E., Janot, J.-M., Chinappi, M.,  
559 Balme, S., 2018a. Amyloid Growth, Inhibition, and Real-Time Enzymatic Degradation

560 Revealed with Single Conical Nanopore. *Analytical chemistry* 90 (21), 12900–12908.  
561 doi:10.1021/acs.analchem.8b03523.

562 Giambianco, N., Coglitore, D., Janot, J.-M., Coulon, P.E., Charlot, B., Balme, S., 2018b.  
563 Detection of protein aggregate morphology through single antifouling nanopore. *Sensors*  
564 and *Actuators B: Chemical* 260, 736–745. doi:10.1016/j.snb.2018.01.094.

565 Giambianco, N., Fichou, Y., Janot, J.-M., Balanzat, E., Han, S., Balme, S., 2020a.  
566 Mechanisms of Heparin-Induced Tau Aggregation Revealed by a Single Nanopore. *ACS*  
567 *sensors* 5 (4), 1158–1167. doi:10.1021/acssensors.0c00193.

568 Giambianco, N., Janot, J.-M., Gubbiotti, A., Chinappi, M., Balme, S., 2020b. Characterization  
569 of Food Amyloid Protein Digestion by Conical Nanopore. *Small Methods* 9, 1900703.  
570 doi:10.1002/smtd.201900703.

571 Gremer, L., Schölzel, D., Schenk, C., Reinartz, E., Labahn, J., Ravelli, R.B.G., Tusche, M.,  
572 Lopez-Iglesias, C., Hoyer, W., Heise, H., Willbold, D., Schröder, G.F., 2017. Fibril  
573 structure of amyloid- $\beta$ (1-42) by cryo-electron microscopy. *Science (New York, N.Y.)* 358  
574 (6359), 116–119. doi:10.1126/science.aao2825.

575 Hayden, K.M., Norton, M.C., Darcey, D., Ostbye, T., Zandi, P.P., Breitner, J.C.S., Welsh-  
576 Bohmer, K.A., 2010. Occupational exposure to pesticides increases the risk of incident  
577 AD: the Cache County study. *Neurology* 74 (19), 1524–1530.  
578 doi:10.1212/WNL.0b013e3181dd4423.

579 Houghtaling, J., List, J., Mayer, M., 2018a. Nanopore-Based, Rapid Characterization of  
580 Individual Amyloid Particles in Solution: Concepts, Challenges, and Prospects. *SMALL*  
581 14 (46, SI). doi:10.1002/sml.201802412.

582 Houghtaling, J., List, J., Mayer, M., 2018b. Nanopore-Based, Rapid Characterization of  
583 Individual Amyloid Particles in Solution: Concepts, Challenges, and Prospects. *Small*

584 (Weinheim an der Bergstrasse, Germany) 14 (46), e1802412.  
585 doi:10.1002/sml.201802412.

586 Hu, R., Diao, J., Li, J., Tang, Z., Li, X., Leitz, J., Long, J., Liu, J., Yu, D., Zhao, Q. Intrinsic  
587 and membrane-facilitated  $\alpha$ -synuclein oligomerization revealed by label-free detection  
588 through solid-state nanopores. *Sci Rep* 6 (1), 1–11. doi:10.1038/srep20776.

589 Huang, G., Voet, A., Maglia, G., 2019. FraC nanopores with adjustable diameter identify the  
590 mass of opposite-charge peptides with 44 dalton resolution. *Nature communications* 10  
591 (1), 835. doi:10.1038/s41467-019-08761-6.

592 Jahn, T.R., Radford, S.E., 2008. Folding versus aggregation: polypeptide conformations on  
593 competing pathways. *Archives of biochemistry and biophysics* 469 (1), 100–117.  
594 doi:10.1016/j.abb.2007.05.015.

595 Ke, P.C., Zhou, R., Serpell, L.C., Riek, R., Knowles, T.P.J., Lashuel, H.A., Gazit, E., Hamley,  
596 I.W., Davis, T.P., Fändrich, M., Otzen, D.E., Chapman, M.R., Dobson, C.M., Eisenberg,  
597 D.S., Mezzenga, R., 2020. Half a century of amyloids: past, present and future. *Chem.*  
598 *Soc. Rev.* 49 (15), 5473–5509. doi:10.1039/c9cs00199a.

599 Lafon, P.-A., Wang, Y., Arango-Lievano, M., Torrent, J., Salvador-Prince, L., Mansuy, M.,  
600 Mestre-Francès, N., Givalois, L., Liu, J., Mercader, J.V., Jeanneteau, F., Desrumaux, C.,  
601 Perrier, V., 2020. Fungicide Residues Exposure and  $\beta$ -amyloid Aggregation in a Mouse  
602 Model of Alzheimer's Disease. *Environmental health perspectives* 128 (1), 17011.  
603 doi:10.1289/EHP5550.

604 Lee, J., Cheng, X., Swails, J.M., Yeom, M.S., Eastman, P.K., Lemkul, J.A., Wei, S., Buckner,  
605 J., Jeong, J.C., Qi, Y., Jo, S., Pande, V.S., Case, D.A., Brooks, C.L., MacKerell, A.D.,  
606 Klauda, J.B., Im, W., 2015. CHARMM-GUI Input Generator for NAMD, GROMACS,  
607 AMBER, OpenMM, and CHARMM/OpenMM Simulations Using the CHARMM36  
608 Additive Force Field. *Journal of Chemical Theory and Computation*, 12(1), 405-413.

609 Journal of Chemical Theory and Computation 12 (1), 405–413.  
610 doi:10.1021/acs.jctc.5b00935.

611 Lepoitevin, M., Jamilloux, B., Bechelany, M., Balanzat, E., Janot, J.-M., Balme, S., 2016.  
612 Fast and reversible functionalization of a single nanopore based on layer-by-layer  
613 polyelectrolyte self-assembly for tuning current rectification and designing sensors. RSC  
614 Adv. 6 (38), 32228–32233. doi:10.1039/C6RA03698H.

615 Lepoitevin, M., Ma, T., Bechelany, M., Janot, J.-M., Balme, S., 2017. Functionalization of  
616 single solid state nanopores to mimic biological ion channels: A review. Advances in  
617 colloid and interface science 250, 195–213. doi:10.1016/j.cis.2017.09.001.

618 Lührs, T., Ritter, C., Adrian, M., Riek-Loher, D., Bohrmann, B., Döbeli, H., Schubert, D.,  
619 Riek, R., 2005. 3D structure of Alzheimer's amyloid-beta(1-42) fibrils. Proceedings of the  
620 National Academy of Sciences of the United States of America 102 (48), 17342–17347.  
621 doi:10.1073/pnas.0506723102.

622 Ma, T., Janot, J.-M., Balme, S., 2020. Track-Etched Nanopore/Membrane: From Fundamental  
623 to Applications. Small Methods, 2000366. doi:10.1002/smt.202000366.

624 Madampage, C., Tavassoly, O., Christensen, C., Kumari, M., Lee, J.S., 2012. Nanopore  
625 analysis: An emerging technique for studying the folding and misfolding of proteins. Prion  
626 6 (2), 116–123. doi:10.4161/pri.18665.

627 Martyushenko, N., Bell, N.A.W., Lamboll, R.D., Keyser, U.F., 2015. Nanopore analysis of  
628 amyloid fibrils formed by lysozyme aggregation. The Analyst 140 (14), 4882–4886.  
629 doi:10.1039/c5an00530b.

630 McLaurin, J., Yang, D.-S., Yip, C.M., Fraser, P.E., 2000. Review: Modulating Factors in  
631 Amyloid- $\beta$  Fibril Formation. Journal of Structural Biology 130 (2), 259–270.  
632 doi:10.1006/jsbi.2000.4289.

633 Merstorf, C., Cressiot, B., Pastoriza-Gallego, M., Oukhaled, A., Betton, J.-M., Auvray, L.,  
634 Pelta, J., 2012. Wild type, mutant protein unfolding and phase transition detected by  
635 single-nanopore recording. *ACS chemical biology* 7 (4), 652–658.  
636 doi:10.1021/cb2004737.

637 Michaels, T.C.T., Šarić, A., Curk, S., Bernfur, K., Arosio, P., Meisl, G., Dear, A.J., Cohen,  
638 S.I.A., Dobson, C.M., Vendruscolo, M., Linse, S., Knowles, T.P.J., 2020. Dynamics of  
639 oligomer populations formed during the aggregation of Alzheimer's A $\beta$ 42 peptide. *Nature*  
640 *chemistry* 12 (5), 445–451. doi:10.1038/s41557-020-0452-1.

641 Michaels, T.C.T., Šarić, A., Habchi, J., Chia, S., Meisl, G., Vendruscolo, M., Dobson, C.M.,  
642 Knowles, T.P.J., 2018. Chemical Kinetics for Bridging Molecular Mechanisms and  
643 Macroscopic Measurements of Amyloid Fibril Formation. *Annual review of physical*  
644 *chemistry* 69, 273–298. doi:10.1146/annurev-physchem-050317-021322.

645 Nougadère, A., Sirot, V., Cravedi, J.-P., Vasseur, P., Feidt, C., Fussell, R.J., Hu, R., Leblanc,  
646 J.-C., Jean, J., Rivière, G., Sarda, X., Merlo, M., Hulin, M., 2020. Dietary exposure to  
647 pesticide residues and associated health risks in infants and young children - Results of the  
648 French infant total diet study. *Environment International* 137, 105529.

649 Oukhaled, G., Mathé, J., Biance, A.-L., Bacri, L., Betton, J.-M., Lairez, D., Pelta, J., Auvray,  
650 L., 2007. Unfolding of Proteins and Long Transient Conformations Detected by Single  
651 Nanopore Recording. *Phys. Rev. Lett.* 98 (15), 158101.  
652 doi:10.1103/PhysRevLett.98.158101.

653 Ouldali, H., Sarthak, K., Ensslen, T., Piguet, F., Manivet, P., Pelta, J., Behrends, J.C.,  
654 Aksimentiev, A., Oukhaled, A., 2020. Electrical recognition of the twenty proteinogenic  
655 amino acids using an aerolysin nanopore. *Nat Biotechnol* 38 (2), 176–181.  
656 doi:10.1038/s41587-019-0345-2.

657 Phillips, J.C., Braun, R., Wang, W., Gumbart, J., Tajkhorshid, E., Villa, E., Chipot, C., Skeel,  
658 R.D., Kalé, L., Schulten, K., 2005. Scalable molecular dynamics with NAMD. *Journal of*  
659 *computational chemistry* 26 (16), 1781–1802. doi:10.1002/jcc.20289.

660 Piguet, F., Ouldali, H., Pastoriza-Gallego, M., Manivet, P., Pelta, J., Oukhaled, A.  
661 Identification of single amino acid differences in uniformly charged homopolymeric  
662 peptides with aerolysin nanopore. *Nat Commun* 9 (1), 1–13. doi:10.1038/s41467-018-  
663 03418-2.

664 Qiu, Y., Lin, C.-Y., Hinkle, P., Plett, T.S., Yang, C., Chacko, J.V., Digman, M.A., Yeh, L.-H.,  
665 Hsu, J.-P., Siwy, Z.S., 2016. Highly Charged Particles Cause a Larger Current Blockage in  
666 Micropores Compared to Neutral Particles. *ACS nano* 10 (9), 8413–8422.

667 Rodriguez-Larrea, D., Bayley, H., 2013. Multistep protein unfolding during nanopore  
668 translocation. *Nature Nanotech* 8 (4), 288–295. doi:10.1038/nnano.2013.22.

669 Roman, J., Jarroux, N., Patriarche, G., Français, O., Pelta, J., Le Pioufle, B., Bacri, L., 2017.  
670 Functionalized Solid-State Nanopore Integrated in a Reusable Microfluidic Device for a  
671 Better Stability and Nanoparticle Detection. *ACS applied materials & interfaces* 9 (48),  
672 41634–41640. doi:10.1021/acsami.7b14717.

673 Sánchez-Santed, F., Colomina, M.T., Herrero Hernández, E., 2016. Organophosphate  
674 pesticide exposure and neurodegeneration. *Cortex* 74, 417–426.  
675 doi:10.1016/j.cortex.2015.10.003.

676 Serra-Batiste, M., Ninot-Pedrosa, M., Bayoumi, M., Gairí, M., Maglia, G., Carulla, N., 2016.  
677 A $\beta$ 42 assembles into specific  $\beta$ -barrel pore-forming oligomers in membrane-mimicking  
678 environments. *PNAS* 113 (39), 10866–10871. doi:10.1073/pnas.1605104113.

679 Soto, C., Pritzkow, S., 2018. Protein misfolding, aggregation, and conformational strains in  
680 neurodegenerative diseases. *Nature neuroscience* 21 (10), 1332–1340.  
681 doi:10.1038/s41593-018-0235-9.



682 Stefureac, R., Waldner, L., Howard, P., Lee, J.S., 2008. Nanopore analysis of a small 86-  
683 residue protein. *Small* (Weinheim an der Bergstrasse, Germany) 4 (1), 59–63.  
684 doi:10.1002/sml.200700402.

685 Tavassoly, O., Lee, J.S., 2012. Methamphetamine binds to  $\alpha$ -synuclein and causes a  
686 conformational change which can be detected by nanopore analysis. *FEBS letters* 586  
687 (19), 3222–3228. doi:10.1016/j.febslet.2012.06.040.

688 Waduge, P., Hu, R., Bandarkar, P., Yamazaki, H., Cressiot, B., Zhao, Q., Whitford, P.C.,  
689 Wanunu, M., 2017. Nanopore-Based Measurements of Protein Size, Fluctuations, and  
690 Conformational Changes. *ACS nano* 11 (6), 5706–5716. doi:10.1021/acsnano.7b01212.

691 Wälti, M.A., Ravotti, F., Arai, H., Glabe, C.G., Wall, J.S., Böckmann, A., Güntert, P., Meier,  
692 B.H., Riek, R., 2016. Atomic-resolution structure of a disease-relevant A $\beta$ (1-42) amyloid  
693 fibril. *PNAS* 113 (34), E4976-84. doi:10.1073/pnas.1600749113.

694 Wang, H.-Y., Ying, Y.-L., Li, Y., Kraatz, H.-B., Long, Y.-T., 2011. Nanopore analysis of  $\beta$ -  
695 amyloid peptide aggregation transition induced by small molecules. *Analytical chemistry*  
696 83 (5), 1746–1752. doi:10.1021/ac1029874.

697 Yu, R.-J., Lu, S.-M., Xu, S.-W., Li, Y.-J., Xu, Q., Ying, Y.-L., Long, Y.-T., 2019. Single  
698 molecule sensing of amyloid- $\beta$  aggregation by confined glass nanopores. *Chem. Sci.* 10  
699 (46), 10728–10732. doi:10.1039/C9SC03260F.

700 Yusko, E.C., Johnson, J.M., Majd, S., Prangko, P., Rollings, R.C., Li, J., Yang, J., Mayer,  
701 M., 2011. Controlling protein translocation through nanopores with bio-inspired fluid  
702 walls. *Nature Nanotech* 6 (4), 253–260. doi:10.1038/nnano.2011.12.

703 Yusko, E.C., Prangko, P., Sept, D., Rollings, R.C., Li, J., Mayer, M., 2012. Single-particle  
704 characterization of A $\beta$  oligomers in solution. *ACS nano* 6 (7), 5909–5919.  
705 doi:10.1021/nn300542q.

706 Zhao, Y., Janot, J.-M., Balanzat, E., Balme, S., 2017. Mimicking pH-Gated Ionic Channels by  
707 Polyelectrolyte Complex Confinement Inside a Single Nanopore. *Langmuir : the ACS*  
708 *journal of surfaces and colloids* 33 (14), 3484–3490. doi:10.1021/acs.langmuir.7b00377.  
709